International Journal of Heat and Technology
Vol. 44, No. 3, June, 2026, pp. 1177-1187
Journal homepage: http://iieta.org/journals/ijht

Numerical Study of Bionic Roots-Based Structure for Mini-Channel Cold Plate in Battery Thermal Management System

James Julian[1*], Rizki Aldi Anggara[1], Adi Winarta[2], Nabila Aprianti[3], Nandy Putra[4], Fitri Wahyuni[1], Riki Hendra Purba[1], Fathin Muhammad Mahdhudhu[5], Elvi Armadani[6]

[1] Department of Mechanical Engineering, Universitas Pembangunan Nasional Veteran Jakarta, Jakarta 12450, Indonesia
[2] Department of Mechanical Engineering, Politeknik Negeri Bali, Denpasar 80361, Indonesia
[3] National Research and Innovation Agency (BRIN), South Tangerang 15314, Indonesia
[4] Applied Heat Transfer Research Group, Department of Mechanical Engineering, Universitas Indonesia, Jakarta 16424, Indonesia
[5] Department of Naval Architecture, Universitas Pembangunan Nasional Veteran Jakarta, Jakarta 12450, Indonesia
[6] Department of Industrial Engineering, Universitas Pembangunan Nasional Veteran Jakarta, Jakarta 12450, Indonesia

Corresponding Author Email: zames@upnvj.ac.id

https://doi.org/10.18280/ijht.440324

Received: 10 April 2026
Revised: 12 June 2026
Accepted: 20 June 2026
Available online: 30 June 2026

Keywords:
discharge rate, electric vehicle, straight-based, roots-based, temperature

ABSTRACT

The transition to electric vehicles (EVs) within tropical regions necessitates a concentrated emphasis on the advancement of battery technology. However, the challenges of extreme environmental conditions demand a reliable thermal management system to prevent thermal degradation and ensure safety. Therefore, this study proposes a bionic mini-channel cold plate with a roots-based configuration. A numerical approach was applied using a localized heat generation model at a discharge rate of 5 C. The thermal management performance of the roots-based structure was evaluated and compared with the conventional straight-based structure at various Reynolds numbers (Re). The results indicated that the roots-based structure configuration with five channels demonstrated superior heat dissipation performance by expanding the effective contact area. It successfully suppressed the maximum temperature (T_{max}) of the battery to 34.65 °C and maintained temperature uniformity with a temperature difference (ΔT) of 4.2 °C. In contrast, the straight-based configuration was only able to suppress T_{max} to 35.08 °C and ΔT to 4.56 °C. However, the roots-based structure generated higher flow resistance, resulting in a pressure drop of up to 2000 Pa, which caused a decrease in the j/f ratio. Nevertheless, this configuration is justified as a necessary trade-off to ensure the thermal safety of the battery.

1. INTRODUCTION

The transportation sector significantly contributes to global greenhouse gas emissions, with Indonesia accounting for 53% of the country's total emissions [1-4]. The transition to electric vehicles (EVs) is a strategic solution to achieve decarbonization targets [5-7]. In general, EVs are primarily powered by Lithium-ion (Li-ion) batteries due to their high energy density, long life cycle, and low self-discharge rate [8, 9]. However, the adoption rate of energy storage systems in Indonesia remains considerably low, primarily attributed to safety concerns associated with these technologies. Li-ion batteries exhibit a marked sensitivity to operating temperatures, resulting in a high potential for self-heating, which can trigger electrical abuse and thermal runaway [10]. As a tropical country, Indonesia's equatorial climate directly exacerbates this thermal vulnerability. Li-ion batteries operate optimally within a narrow temperature range of 25 °C to 40 °C, with a tolerance for temperature variations not exceeding 3 °C to 5 °C [11-13].

Furthermore, most of the population and economic centers in Indonesia are located in coastal and lowland areas with tropical rainforest and tropical monsoon climates, where the average ambient temperature is recorded in the range of 30 °C to 33 °C [14]. Due to the high ambient temperatures, batteries in tropical climates experience much higher thermal stress and are highly susceptible to extreme heat accumulation during operation. Therefore, the development of a Battery Thermal Management System (BTMS) specifically designed to adapt to tropical environments is urgently needed to ensure safety and accelerate EV adoption in these regions.

BTMS can be classified into three different types of cooling mediums, including water-based, liquid-based, and phase change material-based (PCM-based) [15]. Among these three types, liquid-based cooling is the most widely developed method due to its superiority in reducing heat with a high capacity [16-18]. Liquid-based cooling is generally integrated with a cold plate to maximize the heat transfer process from the battery [19]. Therefore, the geometric structure of the channels formed on the cold plate plays a crucial role in ensuring the effectiveness of the thermal management. Monika et al. comprehensively studied the characteristics of a straight mini-channel cold plate by investigating various aspects, including channel width, number of channels, coolant type, flow rate, coolant temperature, ambient temperature, and discharge rate [20]. Regarding geometric factors, the selection of width and number of channels plays a critical role in influencing the resultant pressure drop. While the straight mini-channel cold plate effectively maintains battery temperatures between 25 °C and 40 °C, it is important to consider the need for power consumption compensation.

To address the limitations of the straight channel cold plate, Zhang et al. [21] modified the geometry of the cold plate by implementing inclined channels. The best configuration was found with an inclination angle of 15 °, which was proven to increase thermal effectiveness by up to 79.64%. However, this study was limited because it did not consider the control of battery temperature uniformity. Conversely, Bao et al. [22] used a different approach by proposing a wide straight channel cold plate (WCP), which was directly compared with several complex cold plate structure designs, such as serpentine, bifurcated, and U-turned channels. Although the study revealed that complex channel designs could improve heat transfer performance in cold plates, the WCP was proven to produce the lowest pressure drop. However, the performance of the WCP requires a large volume of coolant, and its performance degrades as the channel width narrows.

The complexity of channel geometry in cold plates escalated considerably with the implementation of a bionic design approach. Zhan et al. [23] proposed a tree-like bionic structure cold plate with the aim of maintaining the optimal operating temperature range in batteries. In addition, Hu [24] applied a bionic sapling-shaped channel cold plate design to overcome the limitations of traditional complex channel cold plates. Both studies demonstrated effective and superior maximum temperature reduction with a uniform temperature distribution. Furthermore, the bionic channel design on the cold plate produces a lower pressure drop compared to traditional models.

Based on the literature review, it is evident that geometric factors are key parameters for ensuring the effectiveness of thermal management performance. Moreover, the bionic channel cold plate design has been proven to be a geometric approach with superior thermal management performance and lower power consumption. However, the development of bionic channel structures is limited due to their complexity, which makes it challenging to find optimal geometric parameters and triggers an increase in flow resistance in the channel. Therefore, this study proposes a simple bionic structure approach using a roots-based mini-channel structure. Additionally, this approach is designed to maintain the effectiveness of battery thermal management performance in tropical environmental conditions. Thus, this study provides a targeted contribution toward producing a reliable and adaptive BTMS.

2. METHOD

2.1 Physical configuration

The physical configuration of the thermal management system proposed in this study consists of a battery cell and a mini-channel cold plate. Figure 1 illustrates the battery model, a commercial prismatic Lithium Iron Phosphate ($LiFePO_4$) cell with a nominal capacity of 7 Ah, utilized as a heat source [25]. In addition, the cold plate is integrated in direct contact, covering the battery's surface area to maximize the heat transfer area.

As a key innovation, this study proposes a roots-based mini-channel cold plate as a battery thermal management strategy based on a bionic structure approach. In nature, the morphology of plant roots has evolved into a branching structure designed to maximize the surface area for water and nutrient absorption. Adopting this natural principle, the mini-channel cooling structure is constructed to resemble a root network to facilitate a more even coolant distribution and expand the heat transfer contact area. To evaluate its performance effectiveness, this study directly compares the roots-based structure with the straight-based mini-channel cold plate. Furthermore, each design strategy is differentiated based on the number of channels, thereby broadening the scope of evaluation for geometric parameters. The structural and geometric parameters of the mini-channel cold plate were detailed in Table 1.

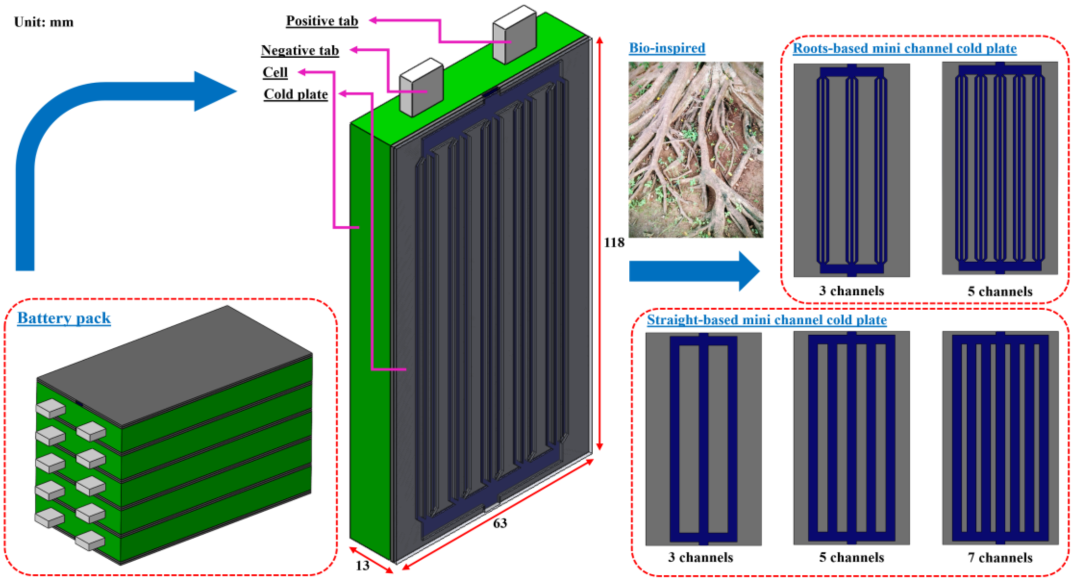

Figure 1. Schematic of the battery and mini-channel cold plate configuration

Table 1. Design mini-channel cold plate parameters

Design Parameter	Unit	Value	Cold Plate Geometries
a	mm	0.5	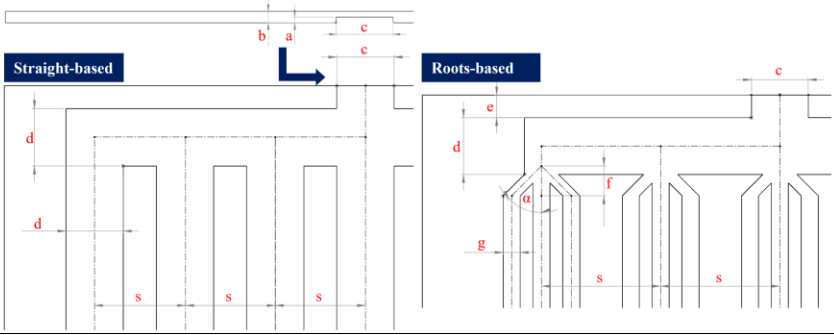
b	mm	1	
c	mm	5	
d	mm	5	
e	mm	2	
f	mm	2.63	
g	mm	1.5	
α	degree	45	
s	mm	15.75; 10.5; 7.875	

2.2 Governing equations

The numerical evaluation was conducted using a Computational Fluid Dynamics (CFD) solver to simulate heat transfer phenomena and fluid dynamics that occur due to the interaction between battery cells, cold plates, and coolant [26]. In the coolant domain, fluid flow dynamics and heat transfer distribution are governed by the principles of mass, momentum, and energy conservation, formulated in Eqs. (1)–(3) [27]. Fluid flow in the cooling channel is assumed to be fully laminar, which is mathematically verified through Eq. (4), the Reynolds number (Re), with the operational constraint that the Re value is kept below 2000 [28].

$$\nabla \bullet \vec{v} = 0 \tag{1}$$

$$\rho_l \left[\frac{\partial \vec{v}}{\partial t} + (\vec{v} \bullet \nabla)\vec{v}\right] = -\nabla p + \mu \nabla^2 \vec{v} \tag{2}$$

$$\rho_l c_{p,l} \frac{\partial T_l}{\partial t} + \nabla \bullet (\rho_l c_{p,l} \vec{v} T_l) = \nabla \bullet (k_l \nabla T_l) \tag{3}$$

$$Re = \frac{\rho_l . U . D_h}{\mu_l} \tag{4}$$

In the context of the discharging process, the battery cell is regarded as a transient volumetric heat source. The temperature distribution and thermal diffusivity phenomena in this battery domain are resolved through the energy conservation regulated by Eq. (5), where Q_{gen} represents the internal heat generation function of the battery [29].

$$\rho_b c_{p,b} \frac{\partial T}{\partial t} = \lambda_{x,b} \frac{\partial^2 T}{\partial^2 x} + \lambda_{y,b} \frac{\partial^2 T}{\partial^2 y} + \lambda_{z,b} \frac{\partial^2 T}{\partial^2 z} + Q_{gen} \tag{5}$$

2.3 Boundary conditions

The thermophysical properties of each component in a single battery pack configuration unit, which includes a battery cell, a cold plate, and water as the coolant, are detailed in Table 2 with the assumption of homogeneous and isotropic materials [25]. The thermal properties of the LiFePO4 cell material were adopted from the study conducted by Rao et al. [30]. The boundary conditions for the numerical domain are illustrated in Figure 2(a). The boundary conditions for the numerical domain are illustrated in Figure 2(a). To minimize computational cost, two symmetry planes were defined on the battery cell and cold plate. In the fluid domain, the inlet was defined as a velocity inlet and the outlet as a zero-pressure boundary. The coolant temperature was set at 30 °C, while the ambient temperature was set at 35 °C to represent the average temperature of tropical climates. The inlet flow velocity was varied within the laminar regime with an interval of 200 ≤ Re ≤ 1400. In addition, a convective heat transfer coefficient of 5 W/m²K was applied to the battery cell surface to model the thermal interaction with the surrounding environment.

Table 2. Thermophysical properties of the Battery Thermal Management System (BTMS) components [25, 30]

	Battery	Aluminum	Water
Density (ρ)	2500 kg/m³	2719 kg/m³	998.2 kg/m³
Specific heat (c_p)	1000 J/kg·K	871 J/kg·K	4182 J/kg·K
Thermal conductivity (**λ**)	3 W/m·K	202.4 W/m·K	0.6 W/m·K
Viscosity (**μ**)	-	-	0.001 Kg m^{-1} s^{-1}

According to the 863 Program recommendations, the maximum charge and discharge rates for Li-ion batteries in EVs can reach 5 C [30]. Such high discharge rates typically occur during demanding driving scenarios, such as rapid acceleration to highway speeds (0–100 km/h) or high-speed overtaking maneuvers [31]. Therefore, the non-uniform temperature distribution during a transient 5 C discharge rate operation was modeled using a localized heat generation approach, as shown in Figure 2(b). Based on the actual battery characteristics experimentally proven by Rao et al. [30], the battery cell was divided into five volume segments with different heat generation profiles [32]. The heat generation in each volume segmentation was governed by Eq. (6), where the value of $Q_{gen(1\text{-}5)}$ was measured based on the actual temperature change rate with time, formulated in Eq. (7). The heat generation characteristics were then approximated by a fitting polynomial function in Eq. (8) to include the influence of thermal diffusivity between volume segments. This calibrated polynomial function was used as an input to construct a User-Defined Function (UDF) that defined the heat source in the battery cell domain [33].

$$Q_{gen(1-5)}(x, y, z, t) = Q_{gen(1-5)}(t) - \lambda_b \nabla^2 T_{b(1-5)} \tag{6}$$

$$Q_{gen(1-5)}(t) = \rho_b c_{p,b} \frac{\Delta T_b}{\Delta t} \tag{7}$$

$$\overline{Q}_{gen(1-5)}(x,y,z,t) = a_{(1-5)}t^3 + b_{(1-5)}t^2 + c_{(1-5)}t + d_{(1-5)} \quad (8)$$

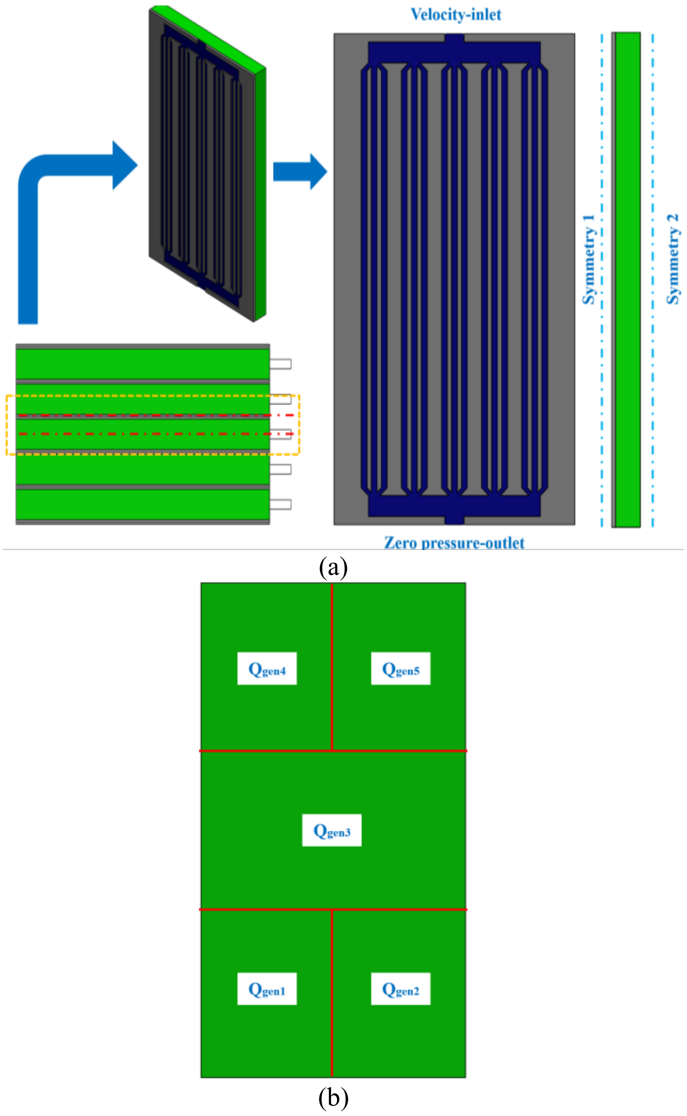

Figure 2. (a) Boundary condition setup; (b) Localized heat generation model

2.4 Performance parameters

The performance of the cooling system was comprehensively evaluated based on thermal indicators, fluid dynamics, and energy consumption efficiency. From a thermal perspective, the primary parameters assessed included the maximum temperature (T_{max}), which is critical in ensuring that the battery operates below its designated thermal limits. Furthermore, the temperature difference (ΔT) was determined using Eq. (9), serving as an indicator of the temperature uniformity within the individual battery cell.

$$\Delta T_b = Tb, min_{b,max} \quad (9)$$

In the hydraulic aspect, the fluid flow resistance in the channel was evaluated using the pressure drop (ΔP) metric defined by Eq. (10). This pressure drop directly affects the pump power requirement (P_{pump}), which was formulated in Eq. (11) as a representation of the power consumption load of the system [23].

$$\Delta P = P_{in} - P_{out} \quad (10)$$

$$P_{pump} = \Delta P . A_{in} . U \quad (11)$$

To analyze the heat transfer effectiveness of roots-based and straight-based channel designs, the thermohydraulic characteristics were examined in greater detail. The parameters of the convective heat transfer coefficient (h_l) and heat dissipated (Q_l) were formulated in Eq. (12) and Eq. (13), respectively, to quantify the rate and capacity of heat dissipation in the fluid.

$$h_l = \frac{Q_l}{A_c \left[T_{b,max} - \frac{(T_{1,in} + T_{1,out})}{2} \right]} \quad (12)$$

$$Q_l = c_p \dot{m} (T_{l,in} - T_{l,out}) \quad (13)$$

In addition, the non-dimensional factor (*j*/*f*) was used to measure the equilibrium of the cooling system's heat dissipation performance against hydraulic resistance. In this case, factor *j* represents the dimensionless heat transfer formulated in Eq. (14), while factor *f* represents the dimensionless hydraulic resistance defined in Eq. (15) [33].

$$j = \frac{Nu}{Re . Pr^{1/3}} \quad (14)$$

$$f = \frac{\Delta P}{\frac{1}{2} . \rho_l . U^2} . \frac{D_h}{4L} \quad (15)$$

$$Nu = \frac{h_l . D_h}{\lambda_l} \quad (16)$$

2.5 Mesh independence test

In the modeled computational domain, an unstructured tetrahedral mesh is used to accommodate complex geometric shapes, as presented in Figure 3. Mesh independence must be ensured during the verification process to maintain numerical accuracy standards. Therefore, this study used the Roache approach to conduct a mesh independence test [34]. Based on the number of elements, the mesh was divided into three samples: fine (8062712 elements), medium (5325945 elements), and coarse (3550703 elements). The quantification of the number of elements in each mesh sample was determined using Eq. (17) with a ratio of r = 1.5.

To test these three mesh samples, this study used the T_{max} and ΔP parameters as indicators of independence in thermal and hydraulic aspects. In determining the quantification error of each mesh, the Grid Convergence Index (GCI) was calculated through Eq. (19) and Eq. (20). Furthermore, the results of the GCI calculation were subjected to a convergence test as defined in Eq. (22). If the convergence test was satisfied, the true value of each parameter could be calculated using Eq. (23). Quantitatively, the mesh independence test results are described in Table 3. Fine mesh was found to be the mesh sample with the lowest error value. In addition, Figure 4 shows that a greater number of mesh elements resulted in a smaller deviation. Thus, fine mesh was used as the numerical specification for the investigation process.

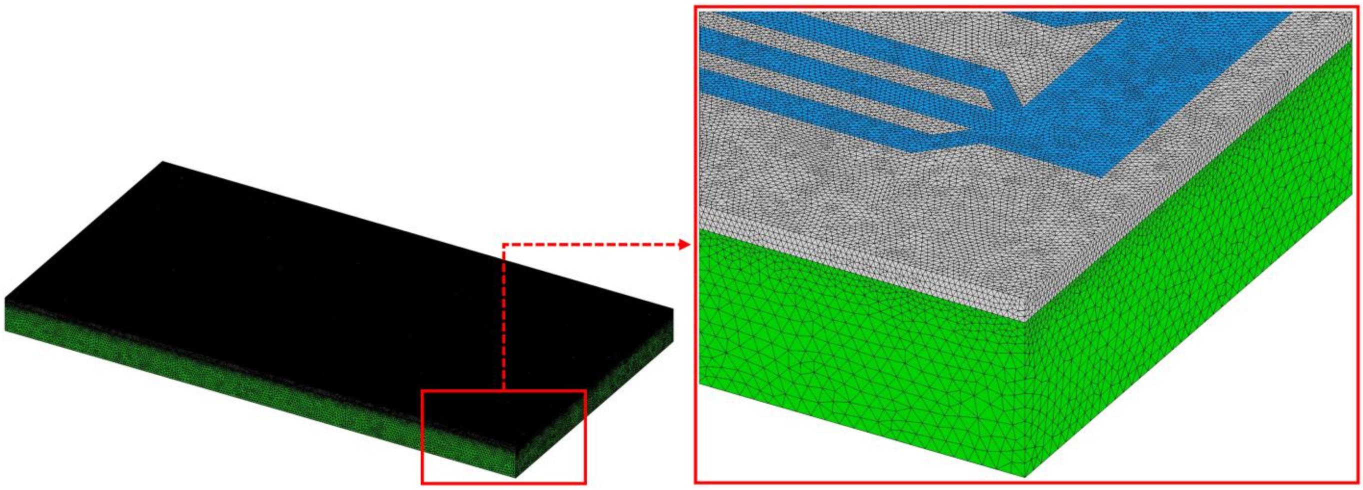

Figure 3. Unstructured tetrahedral mesh

$$r = \frac{h_2}{h_1} \quad (17)$$

$$\overline{p} = \frac{ln\left(\frac{f_3 - f_2}{f_2 - f_1}\right)}{ln(r)} \quad (18)$$

$$GCI_{fine} = \frac{F_s | \in |}{\left(r^{\overline{p}} - 1\right)} \quad (19)$$

$$GCI_{coarse} = \frac{F_s | \in | r^{\overline{p}}}{\left(r^{\overline{p}} - 1\right)} \quad (20)$$

$$\in = \frac{f_{n+1} - f_n}{f_n} \quad (21)$$

$$\frac{GCI_{coarse}}{GCI_{fine} r^{\overline{p}}} \approx 1 \quad (22)$$

$$f\, r_{h=0} = f_1 + \frac{(f_1 - f_2)}{\left(r^{\overline{p}} - 1\right)} \quad (23)$$

Table 3. The result of mesh independence study

Mesh	Fine	Medium	Coarse
		T_{max}	
Value	40.55987	40.56528	40.58463
$\overline{p}$		3.14	
r		1.5	
GCI_{fine}		0.00648%	
GCI_{coarse}		0.02316%	
$f_{rh} = 0$		40.55777	
$\frac{GCI_{coarse}}{GCI_{fine} r^{\overline{p}}}$		1	
Error	**0.00518%**	**0.01853%**	**0.06623%**
		ΔP	
Value	74.39525	73.57719	70.39204
$\overline{p}$		3.35	
r		1.5	
GCI_{fine}		0.47502%	
GCI_{coarse}		1.84953%	
$f_{rh} = 0$		74.67796	
$\frac{GCI_{coarse}}{GCI_{fine} r^{\overline{p}}}$		1	
Error	**0.37858%**	**1.47402%**	**5.73921%**

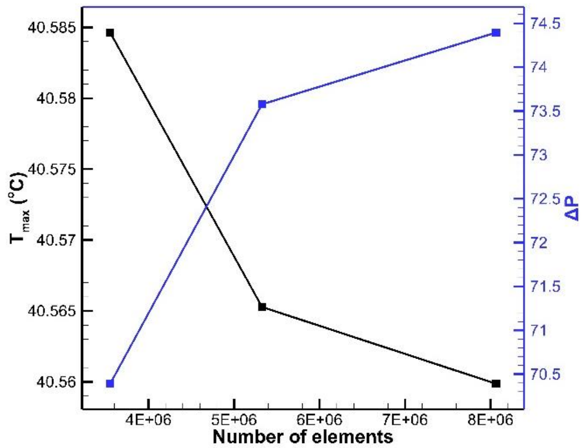

Figure 4. Mesh sensitivity

3. RESULTS AND DISCUSSION

3.1 Validation

Before analyzing the effectiveness of the proposed thermal management system, the accuracy of the numerical model was evaluated during the validation stage. This validation process was carried out by comparing the temperature curve from the numerical simulation results with the experimental data reported by Rao et al. In this comparison, the operational parameters were set to actual conditions, specifically at a discharge rate of 5 C under a constant ambient temperature of 25 °C [30]. Based on the comparison graph shown in Figure 5(a), the simulation results clearly showed a temperature increase trend that was similar to the experimental measurement results at five different measurement point locations. This trend, with a minimal deviation range, strongly indicated that the implemented five-segment heat generation model was valid and highly reliable in capturing the thermal dynamics of the battery. The mean absolute percentage error of the numerical simulation is shown in Figure 5(b).

Furthermore, the spatial characteristics of the thermal phenomena in the battery were visualized through the temperature distribution contours in Figure 5(c). The visualization clearly showed that the temperature profile inside the battery cell during operation at a high discharge rate (5 C) was non-uniform, leading to a spike in temperature differences that exceeded safe operational limits. The highest heat accumulation point was consistently found to be centered in the upper area of the battery, precisely in the area adjacent to the positive tab. This finding fundamentally confirmed that the high concentration of current flow around the terminal area triggered an increase in ohmic resistance, which ultimately produced extreme heat intensity in that localized region. This non-uniform thermal distribution characteristic also provided empirical justification that the placement of cooling strategies must be precisely designed to reduce heat buildup in critical areas of the battery.

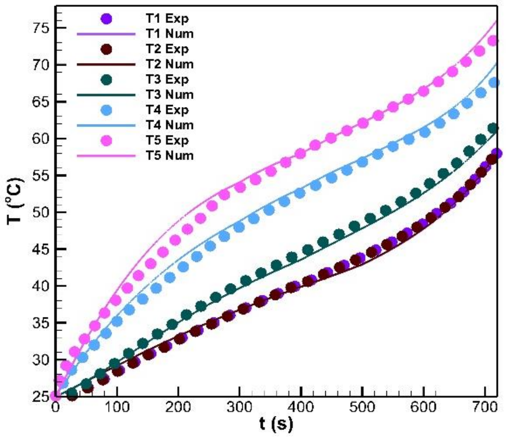

(a)

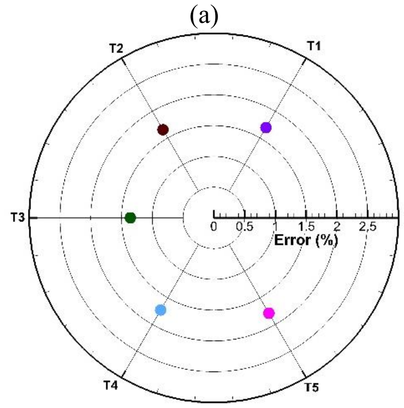

(b)

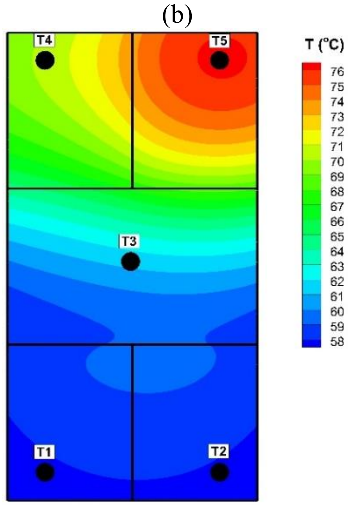

(c)

Figure 5. (a) Numerical validation; (b) Mean absolute percentage error; (c) Temperature distribution of battery

3.2 Analysis

Figure 6 presents the performance of the thermal management system at a constant flow rate (Re = 200), which was comprehensively evaluated by comparing the evolution of the maximum temperature (T_{max}) and the temperature difference (ΔT). In Figure 6(a), the thermal characteristics during the discharge period can be classified into three main phases. In the initial phase (0–100 s), the T_{max} curve showed a sharp increasing gradient due to the dominance of heat generation immediately after the discharge cycle began. At the peak of this phase, the bionic roots-based structure with the largest number of channels successfully reduced the temperature spike to 38 °C, outperforming the straight-based structure, which reached 39 °C. However, an examination of the temperature uniformity in Figure 6(b) revealed that this initial spike instantly triggered an increase in ΔT beyond the safe tolerance limit (≤5 °C). This phenomenon indicated that the fluid convection capacity at Re = 200 was not effective enough to dissipate the local heat concentration, thus creating an extreme spatial temperature gradient imbalance at the beginning of operation.

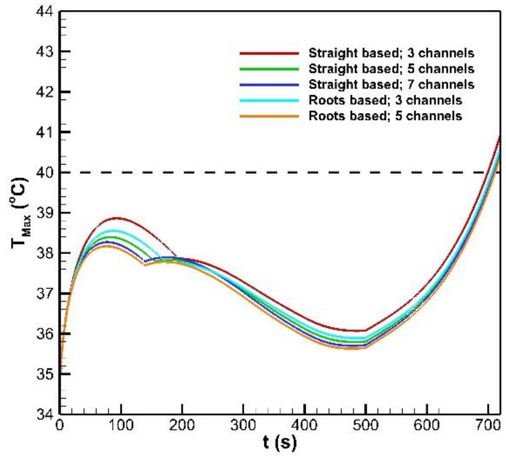

(a)

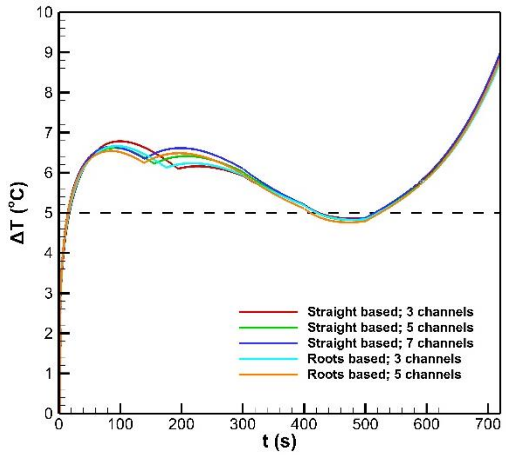

(b)

Figure 6. Battery thermal characteristics at Re = 200: (a) Maximum temperature (T_{max}); (b) Temperature difference (ΔT)

Entering the middle phase (100–500 s), the heat dissipation rate from the coolant circulation gradually began to offset the battery's heat generation. The T_{max} curve exhibited a downward trend, with the roots-based cold plate consistently demonstrating superior performance by maintaining the maximum temperature at a minimum of around 35.5 °C. This temperature suppression significantly affected the thermal balance, as indicated by a decrease in ΔT approaching the safe limit in the 400 to 500 s interval. However, the cooling performance at Re = 200 degraded during the final phase of the discharge cycle. The high increase in Depth of Discharge (DOD) triggered a significant escalation of heat generation. As a result, the T_{max} curve again increased beyond the critical threshold of 40 ℃ in all mini-channel cold plate structure configurations. This cooling system failure was exacerbated by a spike in the ΔT curve beyond the safe operational limit. Overall, the results of the investigation under these conditions confirmed that although the roots-based design offered better heat dissipation effectiveness, it was still inadequate to address battery temperature homogeneity.

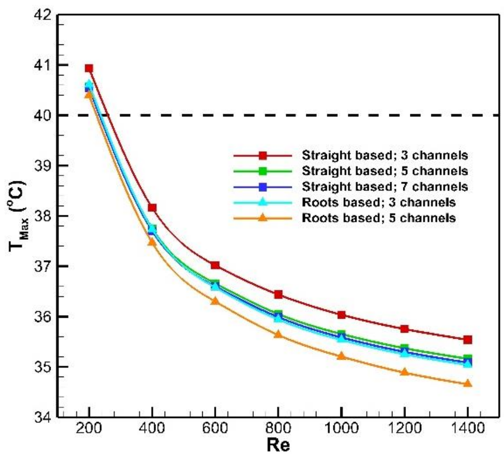

(a)

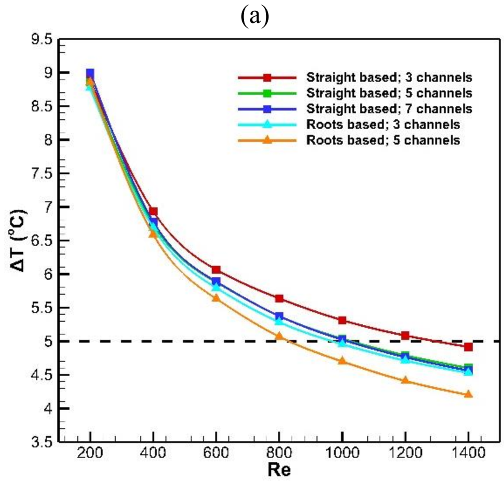

(b)

Figure 7. Battery thermal characteristics with different of Re: (a) Maximum temperature (T_{max}); (b) Temperature difference (ΔT)

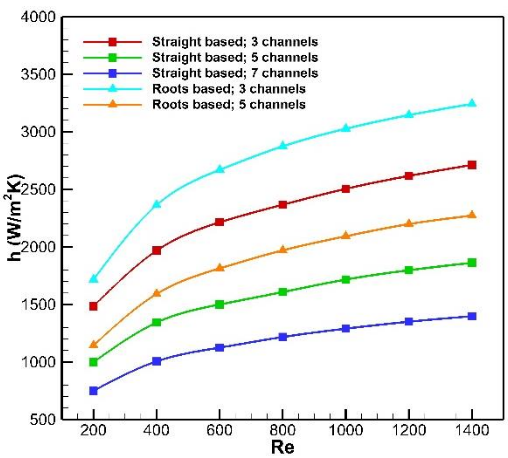

(a)

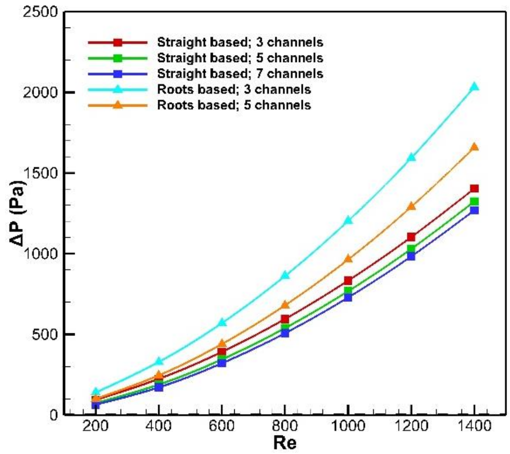

(b)

Figure 8. Performance of cooling system with different Re: (a) Heat transfer coefficient (h); (b) Pressure drop (ΔP)

Furthermore, the influence of Re variations on T_{max} was further investigated, as shown in Figure 7(a). The analysis indicated that the changes in T_{max} began to demonstrate a significant impact at Re = 400. Conversely, the effectiveness of the ΔT profile became clearly evident in the Roots-based configuration with 5 channels at Re = 800. Increasing the flow to Re = 1400 demonstrated that all structural variations of the mini-channel cold plate exhibited satisfactory ΔT performance. However, among the tested variations, the Roots-based with 5 channels design was identified as the superior structural configuration, demonstrating the capability to optimally reduce ΔT by up to 4.2 ℃.

To understand the underlying mechanism of thermal management enhancement and evaluate its hydraulic compensation, the thermohydraulic characteristics of the system were evaluated based on the parameters of the average convective heat transfer coefficient (h_l) and pressure drop (ΔP), as illustrated sequentially in Figure 8. The results of the study indicated that the escalation of Re proportionally strengthened the convective heat transfer while increasing the internal flow resistance in all configurations. From the aspect of heat transfer effectiveness in Figure 8(a), an increasing number of channels implied a decrease in h_l.

At a constant Re, the addition of channels minimized the fluid momentum, thereby reducing the local flow velocity in each branch. However, the bionic roots-based mini-channel cold plate structure consistently validated its superiority by producing superior convective effectiveness compared to the straight-based channel. Branches with smaller hydraulic diameters characterized the root morphology, thus interrupting the growth of the thermal boundary layer. Through this mechanism, the roots-based configuration with 3 channels was proven successful in achieving the highest h_l.

Nonetheless, the hydraulic analysis presented in Figure 8(b) indicated that, despite the superior heat transfer performance of roots-based mini-channel cold plates, they experienced a significantly greater pressure drop in comparison to conventional straight-based structures. The roots-based mini-channel morphology triggered greater internal flow resistance, causing hydraulic losses that resulted in increased pump power consumption, as quantified in Table 4. The roots-based mini-channel cold plate was identified as the configuration with the highest ΔP, reaching more than 2000 Pa, with a pump power consumption reaching 8.58×10^{-3} Watt. However, this loss can be suppressed by increasing the number of channels. Therefore, the straight-based design with 7 channels recorded the lowest ΔP of around 1400 Pa, with a pump power consumption of only 5.36 × 10^{-3} Watt.

In this study, a visualization of the temperature distribution contours of the battery cell at a maximum flow rate (Re = 1400) across all mini-channel cold plate structure configurations is presented in Figure 9. In general, the integration of a mini-channel cold plate triggered a significant thermal redistribution. The concentration of extreme heat accumulation in the terminal area (tabs) was successfully dissipated and distributed towards the bottom cross-section of the cell. However, the structure configuration with a minimum number of channels still showed heat localization, especially in the internal region of the battery cell. This phenomenon confirmed that batteries have very low thermal conductivity. Thus, the effective contact area of this configuration was not enough to maximize heat dissipation in the internal cell under these conditions.

Table 4. Power pump consumption (Watt) of cooling system with different Re

Re	Straight Based			Roots Based	
	3 Channels	5 Channels	7 Channels	3 Channels	5 Channels
200	5.72 × 10^{-5}	4.49 × 10^{-5}	3.93 × 10^{-5}	8.44 × 10^{-5}	6.05 × 10^{-5}
400	2.71 × 10^{-4}	2.28 × 10^{-4}	2.07 × 10^{-4}	3.97 × 10^{-4}	2.97 × 10^{-4}
600	7.08 × 10^{-4}	6.24 × 10^{-4}	5.80 × 10^{-4}	1.03 × 10^{-3}	7.96 × 10^{-4}
800	1.44 × 10^{-3}	1.30 × 10^{-3}	1.22 × 10^{-3}	2.08 × 10^{-3}	1.64 × 10^{-3}
1000	2.51 × 10^{-3}	2.31 × 10^{-3}	2.20 × 10^{-3}	3.63 × 10^{-3}	2.91 × 10^{-3}
1200	3.99 × 10^{-3}	3.72 × 10^{-3}	3.56 × 10^{-3}	5.76 × 10^{-3}	4.67 × 10^{-3}
1400	5.92 × 10^{-3}	5.59 × 10^{-3}	5.36 × 10^{-3}	8.58 × 10^{-3}	7.00 × 10^{-3}

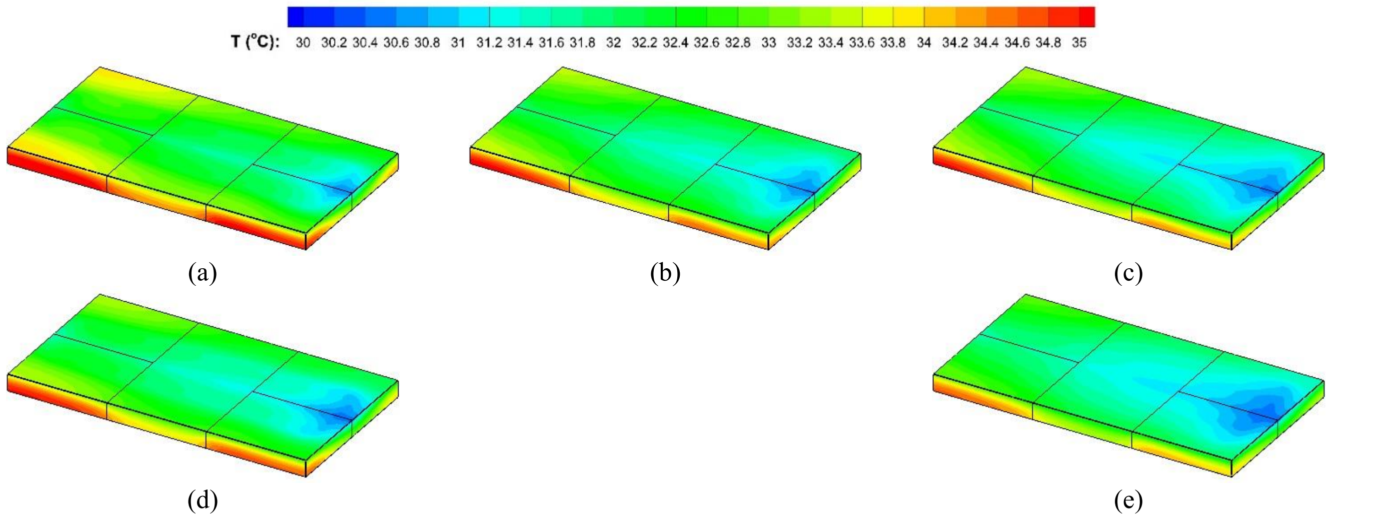

Figure 9. Temperature distribution of battery at Re = 1400: (a) Straight based, 3 channels; (b) Straight based, 5 channels; (c) Straight based, 7 channels; (d) Roots based, 3 channels; (e) Roots based, 5 channels

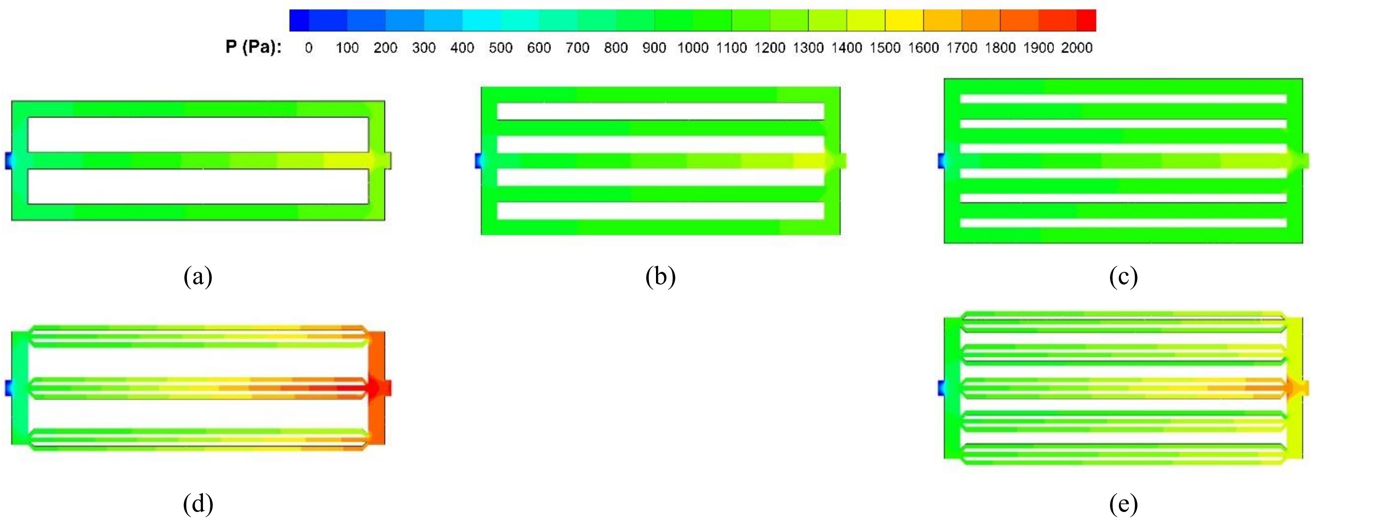

Figure 10. Pressure distribution of mini-channel cold plate at Re = 1400: (a) Straight based, 3 channels; (b) Straight based, 5 channels; (c) Straight based, 7 channels; (d) Roots based, 3 channels; (e) Roots based, 5 channels

In order to enhance thermal management in batteries, it was crucial to augment the number of channels. This expansion not only led to a significant reduction in the maximum temperature observed but also improved the thermal homogeneity across the battery. In addition to increasing the number of channels, reconstructing the mini-channel cold plate structure with a bionic approach was proven to produce superior thermal management performance. The roots-based configuration with 5 channels demonstrated the lowest temperature range with the most uniform distribution. Thus, the roots-based branching morphology facilitated the spread of flow distribution with a more significant effective contact area.

On the other hand, the pressure distribution contour inside the mini-channel cold plate at Re = 1400 is visualized in Figure 10. This visualization illustrates the trade-offs associated with the implementation of bionic structures in relation to the hydraulic load within the cooling system. In the roots-based structure configuration with a minimum number of channels, a dominant high-pressure zone was identified in the upstream area. This phenomenon occurred due to the branching morphology formed with a smaller hydraulic diameter, resulting in a high stagnation pressure zone. In this case, the internal flow resistance was very dominant, triggering significant energy losses. Internal flow resistance was proven to be minimized in the straight-based structure configuration. In addition, increasing the number of channels effectively minimized the intensity of the high-pressure zone on the upstream side. Thus, the straight-based configuration with 7 channels produced the lowest pressure drop.

In addition, the balance between the heat transfer effectiveness enhancement and hydraulic trade-off was holistically evaluated based on the non-dimensional j/f ratio in each mini-channel cold plate structure configuration, as represented in Figure 11. In general, all configurations showed a similar parabolic curve trend. The j/f ratio value escalated in the initial phase and reached a peak point around Re = 400. However, as the flow rate increased, the j/f ratio showed a decreasing trend. This phenomenon indicated that at higher flow rates, the growth of hydraulic resistance due to pressure drop increased more dominantly compared to the heat transfer effectiveness of the cooling system.

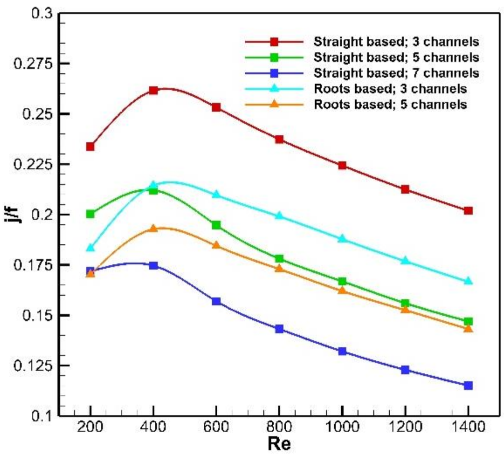

Figure 11. j/f ratio with different Re

Overall, the straight-based configuration recorded a higher j/f ratio compared to the roots-based one in each number of channels. The straight-based variant with 3 channels was identified as the configuration with the highest j/f ratio. Despite having a higher pressure drop compared to a larger number of channels, the configuration showed a more significant average heat transfer, thus maximizing the effectiveness of the mini-channel cold plate. In contrast, roots-based bionic structures tended to produce massive pressure drops, which degraded the overall j/f ratio. However, there was a trade-off between the cooling system's effectiveness and the performance indicators for battery thermal management. While the straight-based configuration with 3 channels appeared effective thermally, it did not meet the battery thermal management performance indicators for maintaining temperature homogeneity below safe thresholds. On the other hand, although the roots-based structure with 5 channels required higher hydraulic load compensation, this configuration could satisfy the battery thermal management performance indicators well at lower flow rates. Therefore, the decrease in the effectiveness of thermohydraulic performance in this roots-based structure provided strong justification as an essential trade-off to ensure the reliability and thermal safety of Li-ion batteries, especially for operational adaptation in extreme tropical climates.

4. CONCLUSION

This study proposed a mini-channel cold plate with a bionic roots-based structure as a Li-ion BTMS to prevent thermal degradation and ensure operational safety in tropical climates. Using a numerical approach, a localized heat generation model accurately captured the phenomenon of non-uniform temperature distribution, where heat accumulation was concentrated in the positive tab area due to the dominance of ohmic resistance during a 5 C discharge cycle. The investigation results demonstrated that the use of a roots-based mini-channel cold plate configuration significantly improved heat dissipation performance by expanding the effective contact area through a bionic branching morphology. The roots-based configuration with 5 channels demonstrated superior performance, successfully suppressing the maximum temperature (T_{max}) to 34.65 °C and satisfying the safe limit of battery temperature homogeneity with a temperature difference (ΔT) of less than 5 °C.

However, the enhanced effectiveness of convective heat transfer (h_l) in this bionic design necessitated significant compensation for the hydraulic load. The complexity of the structural branching induced a stagnation pressure zone in the upstream area, which resulted in a massive pressure drop (ΔP) due to internal flow resistance. A comprehensive thermohydraulic equilibrium evaluation confirmed that the straight-based configuration with 3 channels exhibited the highest j/f ratio. However, this configuration proved ineffective in satisfying thermal management performance in terms of battery temperature homogeneity. On the other hand, the roots-based configuration with 5 channels provided strong justification as an essential trade-off for ensuring a reliable and uniform battery temperature distribution. Nevertheless, the primary limitation of the roots-based mini-channel cold plate approach remains its high pressure drop. Thus, further research is needed to optimize the geometric parameters of the roots-based structure in order to minimize hydraulic losses without sacrificing its superior thermal management effectiveness.

ACKNOWLEDGMENT

This work was supported by the National Research and Innovation Agency (BRIN) through the RIIM LPDP Grant, contract number 133/IV/KS/07/2025. The authors gratefully acknowledge this financial support, which made the successful execution of this research possible and substantially enriched the depth and breadth of the study.

REFERENCES

[1] Hope, J., Yang, H.Y., Gu, M.Y., Fang, C., Li, Y.Z. (2023). Assessing the future trajectory of the China's electric vehicle industry: A mini-review of the greenhouse gas emissions in Beijing and Shenzhen. E3S Web of Conferences, 393: 01037. https://doi.org/10.1051/e3sconf/202339301037

[2] Dwiananto, Y.I., Apriyanto, H., Soehadi, G., et al. (2022). Modeling projection of the number of charging stations and battery electric vehicles until 2030 in Jakarta Indonesia in order to reduce greenhouse gas (GHG) emissions. IOP Conference Series: Earth and Environmental Science, 1108(1): 012024. https://doi.org/10.1088/1755-1315/1108/1/012024

[3] Hill, G., Heidrich, O., Creutzig, F., Blythe, P. (2019). The role of electric vehicles in near-term mitigation pathways and achieving the UK's carbon budget. Applied Energy, 251: 113111. https://doi.org/10.1016/j.apenergy.2019.04.107

[4] Yaacob, N.F.F., Mat Yazid, M.R., Abdul Maulud, K.N., Ahmad Basri, N.E. (2020). A review of the measurement method, analysis and implementation policy of carbon dioxide emission from transportation. Sustainability, 12(14): 5873. https://doi.org/10.3390/su12145873

[5] Hakam, D.F., Jumayla, S. (2024). Electric vehicle adoption in Indonesia: Lesson learned from developed and developing countries. Sustainable Futures, 8: 100348. https://doi.org/10.1016/j.sftr.2024.100348

[6] Veza, I., Abas, M.A., Djamari, D.W., et al. (2022). Electric vehicles in Malaysia and Indonesia: Opportunities and challenges. Energies, 15(7): 2564. https://doi.org/10.3390/en15072564

[7] Nurliyana, C., Lestari, Y.D., Prasetio, E.A., Belgiawan, P.F. (2023). Exploring drivers' interest in different levels of autonomous vehicles: Insights from Java Island, Indonesia. Transportation Research Interdisciplinary Perspectives, 19: 100820. https://doi.org/10.1016/j.trip.2023.100820

[8] Feng, J., He, Y.L., Wang, G.F. (2013). Comparison study of equivalent circuit model of Li-ion battery for electrical vehicles. Research Journal of Applied Sciences, Engineering and Technology, 6(20): 3756-3759. https://doi.org/10.19026/rjaset.6.3587

[9] Ali, A.O., Abdelrehim, O., Saafan, M.M., Elmarghany, M.R., Hamed, A.M. (2025). Comprehensive review of battery management systems for electric vehicles: Thermal management, charging strategies, and emerging technologies. Journal of Power Sources, 658: 238269. https://doi.org/10.1016/j.jpowsour.2025.238269

[10] He, D., Wang, J.L., Peng, Y.J., et al. (2024). Research advances on thermal runaway mechanism of lithium-ion batteries and safety improvement. Sustainable Materials and Technologies, 41: e01017. https://doi.org/10.1016/j.susmat.2024.e01017

[11] Ramshankar, S., Manimozhi, M. (2025). Integration of digital twin technologies for state estimation in electric vehicle batteries: A review. Results in Engineering, 27: 106858. https://doi.org/10.1016/j.rineng.2025.106858

[12] Mammacıoğlu, O., Coskun, G. (2025). A new experimental approach to lithium-ion battery fires in electric vehicles: Investigation of fire behavior and effectiveness of extinguishing agents. Case Studies in Thermal Engineering, 73: 106554. https://doi.org/10.1016/j.csite.2025.106554

[13] Jaguemont, J., Boulon, L., Dubé, Y. (2016). A comprehensive review of lithium-ion batteries used in hybrid and electric vehicles at cold temperatures. Applied Energy, 164: 99-114. https://doi.org/10.1016/j.apenergy.2015.11.034

[14] Paramita, B., Matzarakis, A. (2023). Urban biometeorology of tropical climate: Af, Am, Aw, a propensity of 34 provincial cities in Indonesia. In Climate Change and Cooling Cities. Urban Sustainability. Springer, Singapore, pp. 283-296. https://doi.org/10.1007/978-981-99-3675-5_16

[15] Osaimi, B.A., Ali, H.M. (2026). Review of thermal management strategies for cylindrical lithium-ion batteries: Active, passive, and hybrid approaches. Energy Reports, 15: 108915. https://doi.org/10.1016/j.egyr.2025.12.052

[16] Sharma, A., Khatamifar, M., Lin, W.X., Pitchumani, R. (2024). A state-of-the-art review on numerical investigations of liquid-cooled battery thermal management systems for lithium-ion batteries of electric vehicles. Journal of Energy Storage, 101: 113844. https://doi.org/10.1016/j.est.2024.113844

[17] Qian, Z., Li, Y.M., Rao, Z.H. (2016). Thermal performance of lithium-ion battery thermal management system by using mini-channel cooling. Energy Conversion and Management, 126: 622-631. https://doi.org/10.1016/j.enconman.2016.08.063

[18] Xu, J., Guo, Z.C., Xu, Z.M., Zhou, X., Mei, X.S. (2023). A systematic review and comparison of liquid-based cooling system for lithium-ion batteries. eTransportation, 17: 100242. https://doi.org/10.1016/j.etran.2023.100242

[19] Lan, C.J., Xu, J., Qiao, Y., Ma, Y.B. (2016). Thermal management for high power lithium-ion battery by minichannel aluminum tubes. Applied Thermal Engineering, 101: 284-292. https://doi.org/10.1016/j.applthermaleng.2016.02.070

[20] Monika, K., Chakraborty, C., Roy, S., Dinda, S., Singh, S.A., Datta, S.P. (2021). Parametric investigation to optimize the thermal management of pouch type lithium-ion batteries with mini-channel cold plates. International Journal of Heat and Mass Transfer, 164: 120568. https://doi.org/10.1016/j.ijheatmasstransfer.2020.120568

[21] Zhang, Y.T., Zuo, W., E, J.Q., et al. (2022). Performance comparison between straight channel cold plate and inclined channel cold plate for thermal management of a prismatic LiFePO4 battery. Energy, 248: 123637. https://doi.org/10.1016/j.energy.2022.123637

[22] Bao, Y.H., Shao, S.Q. (2023). Numerical study on ultrathin wide straight flow channel cold plate for Li-ion battery thermal management. Journal of Energy Storage, 64: 107263. https://doi.org/10.1016/j.est.2023.107263

[23] Zhan, S., Que, Y.C., Yin, Y.L., Li, Z.H., Yu, C. (2024).

A novel tree-like bionic structure for liquid-cooled lithium-ion battery plates. International Journal of Thermal Sciences, 203: 109098. https://doi.org/10.1016/j.ijthermalsci.2024.109098
[24] Hu, Y. (2026). Numerical investigation of the battery thermal management system using a bionic sapling – Shaped channel liquid – Cooled plate. International Communications in Heat and Mass Transfer, 171: 110101. https://doi.org/10.1016/j.icheatmasstransfer.2025.110101
[25] Huo, Y.T., Rao, Z.H., Liu, X.J., Zhao, J.T. (2015). Investigation of power battery thermal management by using mini-channel cold plate. Energy Conversion and Management, 89: 387-395. https://doi.org/10.1016/j.enconman.2014.10.015
[26] Ran, Y., Su, Y.F., Chen, L., Yan, K., Yang, C.X., Zhao, Y. (2022). Investigation on thermal performance of water-cooled Li-ion cell and module with tree-shaped channel cold plate. Journal of Energy Storage, 50: 104040. https://doi.org/10.1016/j.est.2022.104040
[27] Tousi, M., Sarchami, A., Kiani, M., Najafi, M., Houshfar, E. (2021). Numerical study of novel liquid-cooled thermal management system for cylindrical Li-ion battery packs under high discharge rate based on AgO nanofluid and copper sheath. Journal of Energy Storage, 41: 102910. https://doi.org/10.1016/j.est.2021.102910
[28] Zhang, D.Y., Yu, Y.J., Yang, W.W., Zhang, X.Q., Yu, C.J., Zhang, Q.F. (2026). Research on the performance of battery thermal management system based on bionic coupling structure and multi-objective optimization. Journal of Energy Storage, 169: 119034. https://doi.org/10.1016/j.est.2025.119034
[29] Liu, H.Q., Ahmad, S., Shi, Y., Zhao, J.Y. (2021). A parametric study of a hybrid battery thermal management system that couples PCM/copper foam composite with helical liquid channel cooling. Energy, 231: 120869. https://doi.org/10.1016/j.energy.2021.120869
[30] Rao, Z.H., Wang, S.F., Zhang, G.Q. (2011). Simulation and experiment of thermal energy management with phase change material for ageing LiFePO4 power battery. Energy Conversion and Management, 52(12): 3408-3414. https://doi.org/10.1016/j.enconman.2011.07.009
[31] Palasai, W., Tepsorn, P., Katthiyawan, T., Srichai, P., Chaopisit, I. (2025). Investigation of the wheel power and state of charge of plug-in hybrid electric vehicles (PHEVs) on a chassis dynamometer in various driving test cycles. Applied Sciences, 15(22): 12320. https://doi.org/10.3390/app152212320
[32] Wang, Z.P., Ma, J., Zhang, L. (2017). Finite element thermal model and simulation for a cylindrical Li-ion battery. IEEE Access, 5: 15372-15379. https://doi.org/10.1109/ACCESS.2017.2723436
[33] Ma, K., Wang, J., Wang, Q.C., Mao, Q.Z. (2025). Numerical simulation of battery thermal management based on ring microchannel cold plate. International Journal of Thermal Sciences, 210: 109563. https://doi.org/10.1016/j.ijthermalsci.2024.109563
[34] Roache, P.J. (1994). Perspective: A method for uniform reporting of grid refinement studies. Journal of Fluids Engineering, 116(3): 405-413. https://doi.org/10.1115/1.2910291

NOMENCLATURE

$\overline{p}$	ordo
A	area, m^2
c_p	specific heat, J/kg.K
D_h	hydraoulic diameter, m
f	non-dimensional friction
GCI	grid convergence index
h	heat transfer coefficient, $W/m^2 \cdot K$
j	non-dimensional heat transfer
L	total length, m
Nu	nusselt number
P	pressure, Pa
Pr	prandlt number
Q	heat dissipated, W
Q_{gen}	heat generation, W/m^3
Re	reynold number
T	temperature, K
U	average velocity
x	x position
y	y position
z	z position

Greek symbols

λ	thermal conductifity, W/m·K
μ	dynamic viscosity, kg/m·s
Δ	difference
ρ	density, kg/m^3

Subscripts

b	batrtery
c	cold plate
in	inlet
l	liquid
max	maximum
min	minimum
out	outlet